Gradual warming prior to the end-Permian mass extinction

by JANA GLIWA[1,2,*] (iD), MICHAEL WIEDENBECK[3], MARTIN SCHOBBEN[4], CLEMENZ V. ULLMANN[5], WOLFGANG KIESSLING[6] (iD), ABBAS GHADERI[7], ULRICH STRUCK[1,8] and DIETER KORN[1,*]

[1]Museum für Naturkunde Berlin, Leibniz Institute for Evolution and Biodiversity Science, Berlin, Germany; jana.gliwa@gmail.com, ulrich.struck@mfn.berlin, dieter.korn@mfn.berlin
[2]Eurasia Department & Beijing Branch Office, German Archaeological Institute, Berlin, Germany
[3]Deutsches GeoForschungsZentrum GFZ, Potsdam, Germany; michael.wiedenbeck@gfz-tsdam.de
[4]Department of Earth Sciences, Utrecht University, Princetonlaan, Utrecht, The Netherlands; schobbenmartin@gmail.com
[5]Camborne School of Mines & Environment and Sustainability Institute, University of Exeter, Exeter, UK; c.ullmann@exeter.ac.uk
[6]GeoZentrum Nordbayern, Friedrich-Alexander University Erlangen-Nürnberg (FAU), Erlangen, Germany; wolfgang.kiessling@fau.de
[7]Department of Geology, Faculty of Science, Ferdowsi University of Mashhad, Mashhad, Iran; aghaderi@um.ac.ir
[8]Institute of Geological Sciences, Freie Universität Berlin, Berlin, Germany
*Corresponding author

Typescript received 12 December 2021; accepted in revised form 13 June 2022

Abstract: The biggest known mass extinction in the history of animal life occurred at the Permian–Triassic boundary and has often been linked to global warming. Previous studies have suggested that a geologically rapid (<40 kyr) temperature increase of more than 10°C occurred simultaneously with the main extinction pulse. This hypothesis is challenged by geochemical and palaeontological data indicating profound environmental perturbations and a temperature rise prior to the main extinction. Using secondary ion mass spectrometry (SIMS), we measured oxygen isotope ratios from Changhsingian (late Permian) ostracods of northwestern Iran. Our data show that ambient seawater temperature began to rise at least 300 kyr prior to the main extinction event. Gradual warming by approximately 12°C was probably responsible for initial environmental degradation that eventually culminated in the global end-Permian mass extinction.

Key words: end-Permian mass extinction, global warming, ostracod, shell calcite, oxygen isotopes, Iran.

THE combination of severe global warming (Joachimski *et al.* 2012, 2019; Schobben *et al.* 2014), the spread of anoxia (Wignall & Twitchett 1996; Penn *et al.* 2018; Schobben *et al.* 2020) and ocean acidification (Jurikova *et al.* 2020) is commonly considered to be the cause of the end-Permian mass extinction (EPME) in marine ecosystems. The ultimate trigger for the environmental changes is thought to be the release of greenhouse gases and volatiles from Siberian Trap volcanism (Cui & Kump 2015; Burgess *et al.* 2017; Clapham & Renne 2019). However, a temporal link between volcanic activity, environmental changes and biological impacts remains controversial.

An initial perturbation of the carbon cycle is first marked by the onset of a decrease in $\delta^{13}C_{carb}$ values recorded in several sections, from marine carbonates approximately 900–650 kyr before the mass extinction horizon (Korte & Kozur 2010; Schobben *et al.* 2017). Zircon-based U/Pb dating of the Siberian Traps indicates that extrusive eruptions and a major portion of the total lava volume were emplaced about 300 kyr before the main extinction pulse (Burgess & Bowring 2015).

However, global warming and peak extinction rate appear to be concentrated in a single interval of <40 kyr duration (Joachimski *et al.* 2012; Burgess *et al.* 2014; Schobben *et al.* 2014; Chen *et al.* 2016; Wang *et al.* 2020). This geologically rapid seawater warming is difficult to reconcile with volcanogenic greenhouse gas emissions that should have initiated global warming much earlier. Here, using oxygen isotope analyses of ostracod shells from a biostratigraphically well-established north-west Iranian section (Gliwa *et al.* 2020), we provide evidence for a much more protracted, earlier warming history.

MATERIAL AND METHOD

Locality and stratigraphy

We studied the well-exposed Permian–Triassic boundary section at the southern side of the Aras Valley (west Azerbaijan, north-west Iran). The section has the geographic coordinates 39.0154°N, 45.4345°E; palaeogeographically, it was situated in an equatorial position on the

Cimmerian microcontinent in the central Tethyan Ocean during the late Permian (Fig. 1). The sediments of this section are all deep shelf deposits below the storm wave base (Leda *et al.* 2014; Gliwa *et al.* 2020). The Aras Valley section has recently been described in detail with respect to its lithology, biostratigraphy, depositional setting, bulk rock $\delta^{13}C$ values and fossil content (Ghaderi *et al.* 2014; Gliwa *et al.* 2020). The section has yielded a series of diverse ostracod assemblages (Gliwa *et al.* 2021).

In the following, we refer to the sample positions according to the distance from the top surface of the red nodular *Paratirolites* Limestone, the top member of the Ali Bashi Formation, and its sharp contact with the shale-dominated Aras Member ('Boundary Clay') of the Elikah Formation. This contact marks the main extinction horizon (Fig. 2).

Rock samples for ostracod extraction were taken from 23 upper Permian to Lower Triassic carbonates and shales of the upper part of the Zal Member, the *Paratirolites* Limestone, the Aras Member and the *Claraia* Beds from −5.60 m to +2.88 m. For the weakly cemented samples from the Aras Member and the lowest part of the *Claraia* Beds (0 to +2.88 m) the ostracod material was extracted by wet sieving with tap water, whereas samples with significant cementation were processed by hot acetolysis (Crasquin-Soleau *et al.* 2005; Gliwa *et al.* 2021). A

comparison of $\delta^{18}O$ values from shell material processed with and without hot acetolysis showed no significant difference of the $\delta^{18}O$ shell values between the different processing methods (Appendix S1).

### Secondary ion mass spectrometry analysis of ostracod shells

We used secondary ion mass spectrometry (SIMS) to measure oxygen isotope compositions of individual spots of 163 ostracod carapaces extracted from the 23 rock samples (Gliwa *et al.* 2022). These carapaces were cast in EpoFix cold-set epoxy resin and polished to a surface topography of better than 10 μm. Each ostracod shell was then imaged using both optical and electron microscopes in order to identify those areas in the shell cross-sections showing the best preservation. Four 25.4 mm-diameter sample mounts were produced, each of which also included numerous grains of the IAEA (International Atomic Energy Agency) 603 calcite reference material (IAEA 2016). The width of the ostracod shell walls on which individual SIMS analyses were carried out ranges between 15 and 30 μm.

The established operating procedure in the Potsdam SIMS is that the samples were ultrasonically cleaned twice for five minutes in high purity ethanol and are then promptly coated with a 35 nm thick high-purity gold coat followed by preparation of an overview image of the entire sample mount using the stitching routine of a Nikon Eclipse motorized optical microscope. These images were then loaded into the SIMS point logger software to support subsequent navigation. The mounts were placed in the instrument after gold coating and they were mostly under vacuum for 12 h or more prior to beginning the analytical routine.

SIMS $\delta^{18}O$ analyses using the Potsdam Cameca 1280-HR employed a *c.* 2 nA, mass filtered $^{133}Cs^+$ beam with a Gaussian density distribution focused to *c.* 5 μm diameter on the polished sample surface. The total impact energy of the Cs^+ ions was 20 keV. Each analysis was preceded by 22 × 22 μm rastered pre-sputter for 70 s. Charge compensation was achieved with low-energy, normal incidence electron flooding. To suppress within-run drift in the isotope ratio, a 17 × 17 μm raster was employed during data acquisition, thus assuring a flat-bottom crater geometry. The rastering of the primary beam during data collection was compensated using the dynamic transfer function of the Cameca 1280's secondary column ion optics. Analyses were performed as multiple points distributed around the best preserved segments of individual ostracods (Appendix S1), and the interior of the majority of the ostracods was also analysed to determine the oxygen isotopic composition of the diagenetic calcite infilling the fossil. The IAEA 603 calcite reference material was

FIG. 1. Geographical and palaeogeographical position (modified after Stampfli & Borel 2002) of the Aras Valley section (red star).
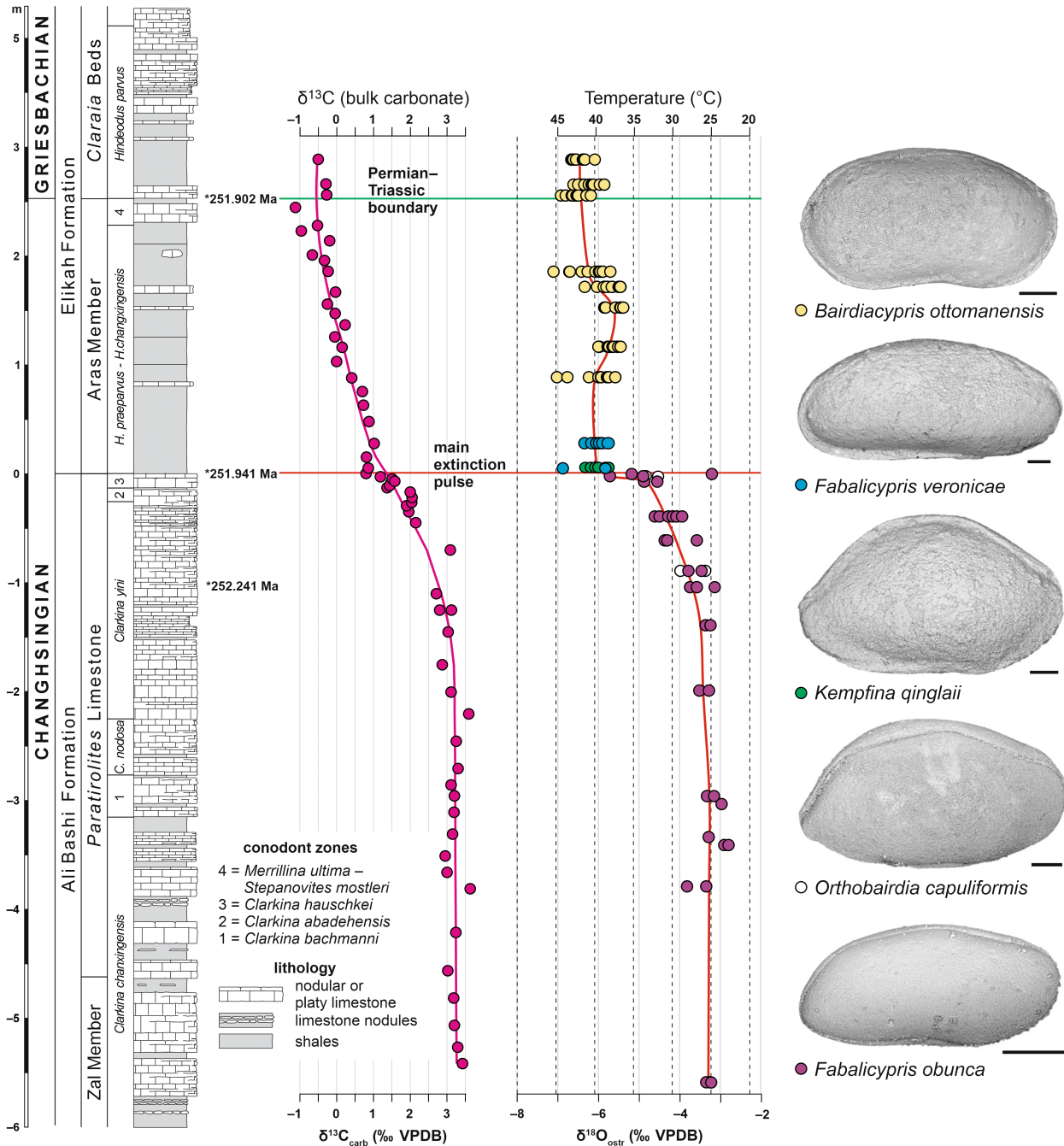
F I G . 2. Aras Valley section with carbon isotope compositions from bulk carbonate and oxygen isotope data from single ostracods. Carbon isotope data from bulk carbonate reported in the standard notation ($\delta^{13}C_{carb}$) relative to Vienna PeeDee Belemnite (VPDB) in per mil from Schobben *et al.* (2017) showing the beginning of the negative excursion in the *Clarkina yini* Zone; $\delta^{18}O_{ostr}$ (‰ VPDB) data from ostracod shell calcite showing a trend largely parallel to the $\delta^{13}C_{carb}$ data. Trendlines represent local polynomial regression fitting (LOESS) with an Akaike's Information Criterion (AIC)-selected optimal smoothing parameter (0.16 for $\delta^{13}C_{carb}$ and 0.22 for $\delta^{18}O_{ostr}$ data). Each datapoint of $\delta^{18}O_{ostr}$ is the arithmetic mean of all shell values measured from a single ostracod specimen. Radiometric ages of the extinction horizon and first appearance of *Hindeodus parvus* at the Induan GSSP (Meishan, South China) from Burgess *et al.* (2014); approximated age of initial decrease of $\delta^{13}C_{carb}$ and $\delta^{18}O_{ostr}$ values based on sediment accumulation rates reported by Schobben *et al.* (2015). Green horizontal line represents the Permian–Triassic boundary with the onset of the *Hindeodus parvus* conodont zone. Conodont zonation from Ghaderi *et al.* (2014). Scale bars of the displayed ostracod species used for the $\delta^{18}O_{ostr}$ analysis represent 100 μm.

analysed after every fifth determination of either ostracod shell wall or sparite infilling, and >30 grains of IAEA 603 were analysed during each overnight automated data acquisition routine.

Secondary ions were accelerated by a -10 kV potential applied to the non-magnetic, stainless sample holder. Prior to the start of data acquisition, the SIMS conducted automated centring routines for the field aperture in both X and Y and for the contrast aperture in X only. The instrument had a field of view of 50×50 μm, in conjunction with a 40 V energy band-pass. The mass spectrometer was operated in static multi-collection mode, with the $^{16}O^-$ ions being collected in the L2' Faraday cup and the $^{18}O^-$ ions being collected in the H2' Faraday cup with the amplifier system employing thermally stabilized 10^{10} Ω and 10^{11} Ω amplifiers, respectively. Magnetic field drift on the mass spectrometer was effectively eliminated by the use of an NMR-controlled feedback loop. The mass resolution of the instrument was determined to be M/ΔM ≈ 1900, which is effectively full transmission for the 1280-HR and suffices to eliminate both the $^{16}O^1H_2$ and the $^{16}O^2H$ isobaric interferences from the ^{18}O mass station. A single analysis consisted of 20 integrations of 4 s each, resulting in a data collection time of 80 s per analysis, equivalent to a total of $c.$ 3 min per point when including the sample moving, pre-sputtering and automatic centring routines. This analytical design resulted in a count rate generally in the range of 2.8 to 3.2×10^9 ions per second on the ^{16}O mass station. A total of 669 $\delta^{18}O$ determinations were made on 163 ostracods specimens. Our SIMS analytical data were collected during three overnight runs in June 2018 and one overnight run in February 2019. A 3SD filter was applied to all data with respect to the 20 individual integrations made during a given analytical run.

In order to quantify the instrumental mass fractionation and also to monitor the possible presence of a time-dependent drift during our run sequences, periodic analyses of the IAEA 603 calcite reference material were made. None of the four days showed evidence of significant time-dependent drift. For the purpose of calibrating the instrumental mass fractionation of our SIMS instrument on each separate day for IAEA-603, we used the value of $\delta^{18}O_{VPDB} = -2.37$ (IAEA 2016). For the four days of data collection, we recorded 1 s repeatabilities for our reference material of $\pm 0.16‰$ (n = 38), $\pm 0.14‰$ (n = 33), $\pm 0.19‰$ (n = 34), and $\pm 0.14‰$ (n = 43). We assigned the zero-point of the VPDB scale to the absolute isotope ratio of $^{18}O/^{16}O = 0.0020672$ (IAEA 1993), which was used to calculate the absolute isotopic fractionation of our experimental process as well as to determine the $\delta^{18}O_{VPDB}$ values of each of our analyses on the ostracods or their spar infillings. Based on the above observations, we assume that our data are reliable at the 0.2‰ (1SE) level, or better.

Temperature reconstruction using oxygen isotopes from ostracod calcite ($\delta^{18}O_{ostr}$)

For temperature reconstruction based on ostracod calcite values ($\delta^{18}O_{ostr}$), we used the equation of Kim & O'Neil (1997) for the temperature-dependent oxygen isotope fractionation during calcite precipitation. Of the entire pool of SIMS data, only those 605 $\delta^{18}O_{ostr}$ values that were assessed to not have been influenced by diagenetic alteration (Appendix S1) were used for our subsequent temperature reconstructions. The oxygen isotope value of the ambient seawater ($\delta^{18}O_{sw}$), which is needed for this equation, can only be assumed for the late Permian to the Early Triassic. For estimating the $\delta^{18}O_{sw}$ value for the sections in north-west Iran, we followed the calculations of Schobben et al. (2014). These estimates are based on $\delta^{18}O_{sw}$ calculations from the equation in Watanabe et al. (2001), using salinity values which were modelled for late Permian seawater by Kiehl & Shields (2005). The resulting $\delta^{18}O_{sw}$ value was shifted by $-1‰$ based on the assumption of an ice-free world for this time interval (Lhomme et al. 2005), resulting in a $\delta^{18}O_{sw}$ value of $-0.81‰$ VPDB for the north-west Iranian sections.

RESULTS

Reconstruction of seawater temperatures at the Permian–Triassic boundary

As it was impossible to separate the ostracod shell material from the sparitic infill, we used secondary ion mass spectrometry (SIMS) to analyse the oxygen isotopic composition of these shells ($\delta^{18}O_{ostr}$). By using this method it was possible to obtain oxygen isotope values for a succession of deep shelf sediments (deposited below the storm wave base) spanning the end-Permian mass extinction; our results are superimposed over a longer term, gradual latest Permian $\delta^{13}C_{carb}$ negative excursion (Gliwa et al. 2020).

Ostracod shells consist of low-Mg calcite, which is relatively stable against diagenetic alteration (Brand & Veizer 1981). Furthermore, there are no signs in the sedimentary succession of the studied section from other nearby sites to suggest subaerial exposure. This minimizes the probability that meteoric fluids (with a distinct $\delta^{18}O$) left an imprint in the calcite shells during early diagenesis. Furthermore, the conodont alteration index (CAI; Königshof 1992) of 1–1.5 at this site and nearby locations (Zal and Ali Bashi; Schobben et al. 2014) suggest minimal thermal overprinting during subsequent burial. Taken together, these are important criteria for the analysis of oxygen isotopes and a temperature reconstruction of the

ambient seawater. Distinct differences of δ^{18}O values from ostracods and the diagenetic endmembers (bulk carbonate and sparite cements) of the same sediments as well as a mineralogical analysis of the ostracod shells support that our measured $\delta^{18}O_{ostr}$ values are unlikely to have been influenced by diagenesis (Appendix S1). Instead, the spatially resolved SIMS δ^{18}O measurements confirmed that altered shell areas or crusts were avoided, thus yielding reliable palaeoenvironmental proxies.

Previous estimates of Permian–Triassic seawater temperature were based on the oxygen isotopic composition of conodont apatite (Joachimski et al. 2012, 2019; Chen et al. 2013, 2016; Schobben et al. 2014) and brachiopod calcite (Korte et al. 2005; Wang et al. 2020). Oxygen isotope ratios may also provide relative temperature differences for the seawater in which the ostracods lived, given prior knowledge of the seawater oxygen isotope compositions (e.g. Von Grafenstein et al. 1999; Hunt et al. 2010; Decrouy et al. 2011; Devriendt et al. 2017), although this tool has not previously been used for temperature reconstructions across the Permian–Triassic boundary.

Permian–Triassic ostracod-based δ^{18}O values and seawater temperatures

The $\delta^{18}O_{ostr}$ (VPDB) values from the Changhsingian to early Griesbachian succession range from −8.3‰ to −2.5‰. The LOESS regression curve (Fig. 2) indicates relatively stable $\delta^{18}O_{ostr}$ values of around −3.3‰ up to the middle *Clarkina yini* Zone, followed by a decrease to around −6‰ in the lowest strata above the extinction horizon. Converting the $\delta^{18}O_{ostr}$ values to temperatures using a $\delta^{18}O_{sw}$ value of −0.81‰ (VPDB) suggests that the temperatures of the ambient seawater were relatively stable at 27°C in the Changhsingian up to the *C. yini* Zone. Seawater temperatures gradually increased to nearly 40°C at the horizon of the main extinction pulse. In the post-extinction interval and persisting into the earliest Triassic the seawater temperature remained relatively high (38–42°C). The $\delta^{18}O_{ostr}$ curve up to the extinction horizon runs almost parallel to the $\delta^{13}C_{carb}$ curve. Our $\delta^{18}O_{ostr}$ values suggest that the initial temperature rise in the latest Permian coincided with the onset of the $\delta^{13}C_{carb}$ decline in the same section (Fig. 2), which has been taken as the onset of major volcanic activity in the Siberian Traps (Burgess & Bowring 2015). Correlation with the conodont zonation and accumulation rates from other north-west Iranian sections spanning the Permian–Triassic boundary (Richoz et al. 2010; Schobben et al. 2015) provides solid evidence that the warming trend commenced some 300 kyr before the main extinction event.

Biases on temperature calculation using biogenic materials

Vital effects are a well-known issue when using ostracods as temperature proxy (e.g. Von Grafenstein et al. 1999; Decrouy et al. 2011; Devriendt et al. 2017). Small differences between $\delta^{18}O_{ostr}$ and the predicted δ^{18}O values of the calcite that precipitates in equilibrium with the surrounding water ($\delta^{18}O_{eq}$) led to the conclusion that vital effects caused by the metabolism of the animal must be taken into account when reconstructing ancient temperatures (Von Grafenstein et al. 1999; Holmes & Chivas 2002; Decrouy et al. 2011). Such vital effects induce the preferential uptake of the ^{18}O isotope (Xia et al. 1997) and generally result in higher $\delta^{18}O_{ostr}$ compared to $\delta^{18}O_{eq}$ (vital offset: $\Delta^{18}O_{ostr-eq}$). These kinetic effects are also influenced by the $[(CO_3)^{2-}]/[DIC]$ ratio of the host water (DIC, dissolved inorganic carbon), which in turn is influenced by the pH and salinity of the water (Devriendt et al. 2017). We calculated the possible impact of pH changes which are proposed for late Permian seawater (Clarkson et al. 2015; Jurikova et al. 2020) on our $\delta^{18}O_{ostr}$ values. This test indicates that the theoretical difference between $\delta^{18}O_{ostr}$ values resulting from pH changes are below the uncertainty estimates of our SIMS analyses (Appendix S1).

Vital offsets are also taxon dependent, hence we have limited our analysis to the few species *Fabalicypris obunca* Belousova, 1965, *Orthobairdia capuliformis* Gliwa in Gliwa et al., 2020, *Fabalicypris veronicae* Gliwa in Gliwa et al., 2020, *Bairdiacypris ottomanensis* Crasquin-Soleau in Crasquin-Soleau et al., 2004 and *Kempfina qinglaii* (Crasquin in Crasquin et al., 2008), which all belong to the family Bairdiidae. The vital offset for ostracods has been measured for several (mostly freshwater) species where it ranges from +0.7‰ to +3.5‰ (e.g. Von Grafenstein et al. 1999, Holmes & Chivas 2002, Decrouy et al. 2011). For the few marine species examined so far, also belonging to the family Bairdiidae, the vital offset is approximately +0.3‰ (Bornemann et al. 2012). A correction for this δ^{18}O offset would lead to systematically higher palaeotemperature estimates. For example, a correction for a constant offset of +0.3‰, which was estimated for the marine species *Bairdia conformis* and *Henryhowella sarsii* (Bornemann et al. 2012) in comparison to $\delta^{18}O_{eq}$, would lead to a positive shift ($\Delta T = T_{eq} - T_{vital}$) of the reconstructed temperature (T_{vital}) of approximately 1.4°C at lower temperatures to 1.7°C at higher temperatures (using the equation of Kim & O'Neil 1997).

The ostracod-based temperature curve is compiled from different species, not taking a possible species-dependent vital offset into account. However, our major result of a pre-extinction temperature rise of c. 10°C is based on the single species *Fabalicypris obunca*. This focus eliminates the risk of a potential species-specific δ^{18}O

bias. Although the reconstruction of the absolute temperatures is hindered by a possible vital offset in $\delta^{18}O$ for *F. obunca*, our trend can confidently be attributed to relative temperature changes, as the vital effect leads to an almost constant offset of $\delta^{18}O$ values in the ostracod shell.

In general, our calculated absolute seawater temperatures are relatively high and partly not compatible with marine life. As the calculation of ancient seawater temperatures depends also on the precise knowledge of the $\delta^{18}O$ values of the seawater, the resulting temperature reconstruction remains an estimation. The $\delta^{18}O_{sw}$ values used in this study are based on salinity reconstructions of late Permian seawater (Kiehl & Shields 2005) and the assumption of an ice-free world (Lhomme *et al.* 2005, Schobben *et al.* 2014). However, these $\delta^{18}O_{sw}$ values remain an estimation and cannot be determined exactly. An overestimation of this value would lead to higher calculated temperature, which could be an explanation for the unrealistic high values in our study.

Permian–Triassic temperature reconstructions from north-west Iran and South China

The magnitude of the ostracod-derived end-Permian temperature increase in the Aras Valley section resembles temperature reconstructions from other Transcaucasian and South Chinese sections (Fig. 3B–E). All conodont-based $\delta^{18}O$ data from these regions indicate a seawater warming of 7–12°C (Joachimski *et al.* 2012, 2019; Chen *et al.* 2013, 2016; Schobben *et al.* 2014; Wang *et al.* 2020). However, only our ostracod-based $\delta^{18}O$ data suggest a clear gradual pre-extinction warming extending over 300 kyr, which was succeeded by a step-change in temperature immediately below the main extinction pulse (Figs 2, 3B, S3). On the other hand, brachiopod-based $\delta^{18}O$ data from north-west Iran (Schobben *et al.* 2014) indicate stable temperatures in the pre-extinction phase of the late Permian (Fig. 3D). A gradual pre-extinction warming, as indicated by the ostracod-based data, was also suggested from brachiopod data in South China (Wang *et al.* 2020), but this observation is based on a very limited number of specimens in this key time interval. Studies of conodont $\delta^{18}O_{apatite}$ from Shangsi (Joachimski *et al.* 2012; Chen *et al.* 2016) suggest a temperature increase of approximately 12°C (from about 25.5 to 37.5°C), thus resembling the data from Meishan. However, the onset of warming is not conspicuous, as the large dispersion in the data in the upper three metres of the pre-extinction interval does not allow the definition of a clear starting point (Fig. 3E). A pre-extinction warming at Shangsi cannot be excluded from these $\delta^{18}O_{apatite}$ values.

There are two plausible explanations for why previous investigations have not provided clear evidence of a gradual pre-extinction warming:

1. Ostracods are benthic organisms and hence more likely to record deeper water column temperatures compared to conodonts that are nektonic and may more closely track sea surface temperatures (Joachimski *et al.* 2012). The ostracod $\delta^{18}O$ values from north-west Iran reflect bottom temperatures of the deep shelf. In general, deep-water temperatures are considered sensitive tracers of global climate change, whereas sea-surface temperatures are more erratic in nature (Westerhold *et al.* 2020). As such, although substantial pre-extinction warming is currently only reported from the Aras Valley (north-west Iran) and Xikou (South China; Wang *et al.* 2020) sections, these probably record a global trend.

2. $\delta^{18}O$ values of biogenic materials (calcite, apatite) record the $\delta^{18}O$ composition of the ambient sea water and a temperature-dependent oxygen isotope fractionation associated with mineral precipitation. The mobility of ostracods is very limited, which enables a precise reconstruction of their ambient temperature. In contrast, conodonts are mobile, nektonic animals, which makes the pin-pointing of their habitat rather difficult.

Timing of environmental and biotic changes at the Permian–Triassic boundary

The environmental changes culminating in the end-Permian mass extinction are commonly assumed to have been triggered by Siberian Trap magmatism (Reichow *et al.* 2002; Kidder & Worsley 2004; Svensen *et al.* 2009; Burgess & Bowring 2015; Bond & Grasby 2017; Burgess *et al.* 2017). For instance, the onset of the global trend towards lower $\delta^{13}C_{carb}$ values is thought to have been induced by volcanic greenhouse gas emissions and combustion of organic-rich sediments and evaporites due to sill intrusions and the subsequent release of ^{13}C-depleted thermogenic gases (Burgess *et al.* 2017; Schobben *et al.* 2019). A comparison of various Permian–Triassic sections demonstrates that this trend had already started several hundred thousand years prior to the extinction, in the *Clarkina bachmanni* conodont zone (Korte & Kozur 2010; Schobben *et al.* 2017). The age model of Schobben *et al.* (2015) suggests that the sediments in the middle of the *C. bachmanni* Zone were deposited approximately 900 kyr before the main extinction horizon. Investigations from the Aras Valley (Schobben *et al.* 2017; Gliwa *et al.* 2020) and other north-west Iranian sections (Schobben *et al.* 2014) indicate a slightly later $\delta^{13}C_{carb}$ decrease, which started in the *C. yini* Zone
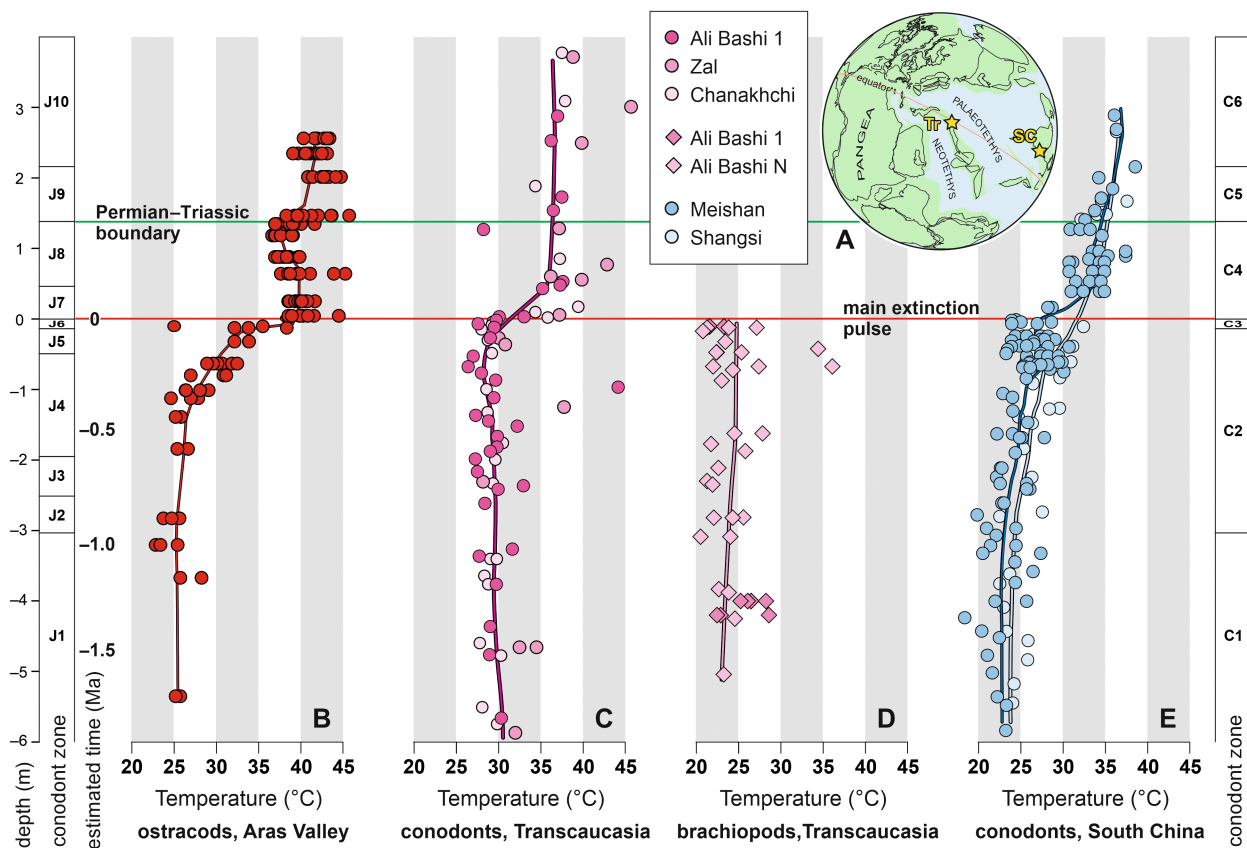
FIG. 3. Palaeotemperature estimates from oxygen isotope data at the end-Permian mass extinction. Depths transcribed to align with the Ali Bashi 1 section, where time before main extinction pulse has been estimated from sediment accumulation rates (Schobben *et al.* 2015). Conodont zones after Ghaderi *et al.* (2014). A, map showing palaeogeographical positions of Transcaucasia (Tr) and South China (SC) (modified after Stampfli & Borel 2002). B–E, temperature derived from: B, $\delta^{18}O$ data from ostracod shell calcite from Aras Valley (this study); C, $\delta^{18}O$ data from conodont apatite from Armenia and north-west Iran (Schobben *et al.* 2014; Joachimski *et al.* 2019) (Appendix S1, p. 6); D, $\delta^{18}O$ data from brachiopod calcite from north-west Iran (this study and Schobben *et al.* (2014); Appendix S1, pp 5, 7); E, $\delta^{18}O$ values from conodont apatite from South China (Joachimski *et al.* 2012; Chen *et al.* 2013; Chen *et al.* 2016) (Appendix S1, p. 7). LOESS smoothing as in Figure 2 (smoothing parameters for temperature values: 0.26 for conodonts from Ali Bashi, 0.91 for brachiopods from Ali Bashi, 0.20 for conodonts from Meishan, 0.46 for conodonts from Shangsi). Conodont zonation in north-west Iran from Ghaderi *et al.* (2014): J1, *Clarkina changxingensis* Zone; J2, *C. bachmanni* Zone; J3, *C. nodosa* Zone; J4, *C. yini* Zone; J5, *C. abadehensis* Zone; J6, *C. hauschkei* Zone; J7, *Hindeodus praeparvus–Hindeodus changxingensis* Zone; J8, *Merrillina ultima–Stepanovites mostleri* Zone; J9, *Hindeodus parvus* Zone; J10, *Isarcicella staeschei* Zone. Conodont zonation in South China from Yuan *et al.* (2014): C1, *C. changxingensis* Zone; C2, *C. yini* Zone; C3, *C. meishanensis* Zone; C4, *Hindeodus praeparvus–Hindeodus changxingensis* Zone; C5, *Hindeodus parvus* Zone; C6, *Isarcicella staeschei/Isarcicella isarcica* Zone.

(Fig. 2), 850–650 kyr before the extinction. These relatively small discrepancies of first occurrences of conodont species are probably caused by incomplete sampling and the fact that fossil occurrence data are influenced by varying accumulation rates, intervals of condensation and minor unconformities (Holland & Patzkowsky 2015).

The timing of the initial $\delta^{13}C_{carb}$ decrease in the north-west Iranian sections is in stark contrast to the $\delta^{13}C_{carb}$ decrease in Meishan, which is assumed to have started only around 60 kyr before the main extinction (Burgess *et al.* 2014). As the duration of the pre-extinction

conodont zones in Meishan are in contrast to the mean accumulation rates covering these zones in the Iranian section, we refer and interpolate all data to the north-west Iranian sections. Volcanic activity and thus carbon cycle disturbances started earlier than the carbon isotope data from Meishan suggest. This is also supported by volcanic fly ash deposits from the Arctic highlands of Canada, which suggest that explosive volcanic eruptions occurred about 750–500 kyr before the main extinction interval (Grasby *et al.* 2011).

Palaeontological data from north-west Iran and South China show that the volcanically induced environmental

changes affected life well before the main mass extinction pulse. An extinction pulse of ammonoids as well as a decline in morphological complexity (size reduction, loss of coarse sculpture, simplification of suture lines) were observed in the *Clarkina nodosa* Zone (Korn *et al.* 2016; Kiessling *et al.* 2018), which corresponds to approximately 750 kyr before the extinction at the Iranian sections (Schobben *et al.* 2015).

Zircon-derived U/Pb dating of the Siberian Traps indicates that the emplacement of around two-thirds of the total lava volume and extrusive eruptions had already started some 300 kyr prior to the extinction (Burgess & Bowring 2015; Burgess *et al.* 2017). This timing also corresponds to the timing of enhanced chemical weathering in Meishan, induced by the emplacement of fresh basalt together with CO_2 release, acid rains and global warming (Sun *et al.* 2018). This coincides exactly with our initial $\delta^{18}O_{ostr}$ decrease and might indicate a linkage between early greenhouse gas emissions from the Siberian Traps

and an increase in deep shelf seawater temperature approximately 300 kyr before the extinction.

A pre-extinction temperature increase that lasted around 300 kyr as indicated by the initially gradual decline of $\delta^{18}O_{ostr}$ values is likely to have caused significant environmental and ecological perturbations prior the main extinction interval. Seawater temperature increase reduces the solubility of oxygen in ocean water and, together with a higher metabolic oxygen demand of organisms (Pörtner 2001), leads to thermal stress and hypoxia (e.g. Benton 2018). Furthermore, ammonoid diversity data from north-west Iran show an extinction pulse within the *C. yini* conodont zone (Kiessling *et al.* 2018), which corresponds to the beginning of rising seawater temperatures (Fig. 4). Gradual warming over c. 300 kyr prior to the main extinction event in the latest Permian may have already induced biological turmoil.

Our oxygen isotope data from ostracod shells in the 8 cm immediately below the extinction horizon support a
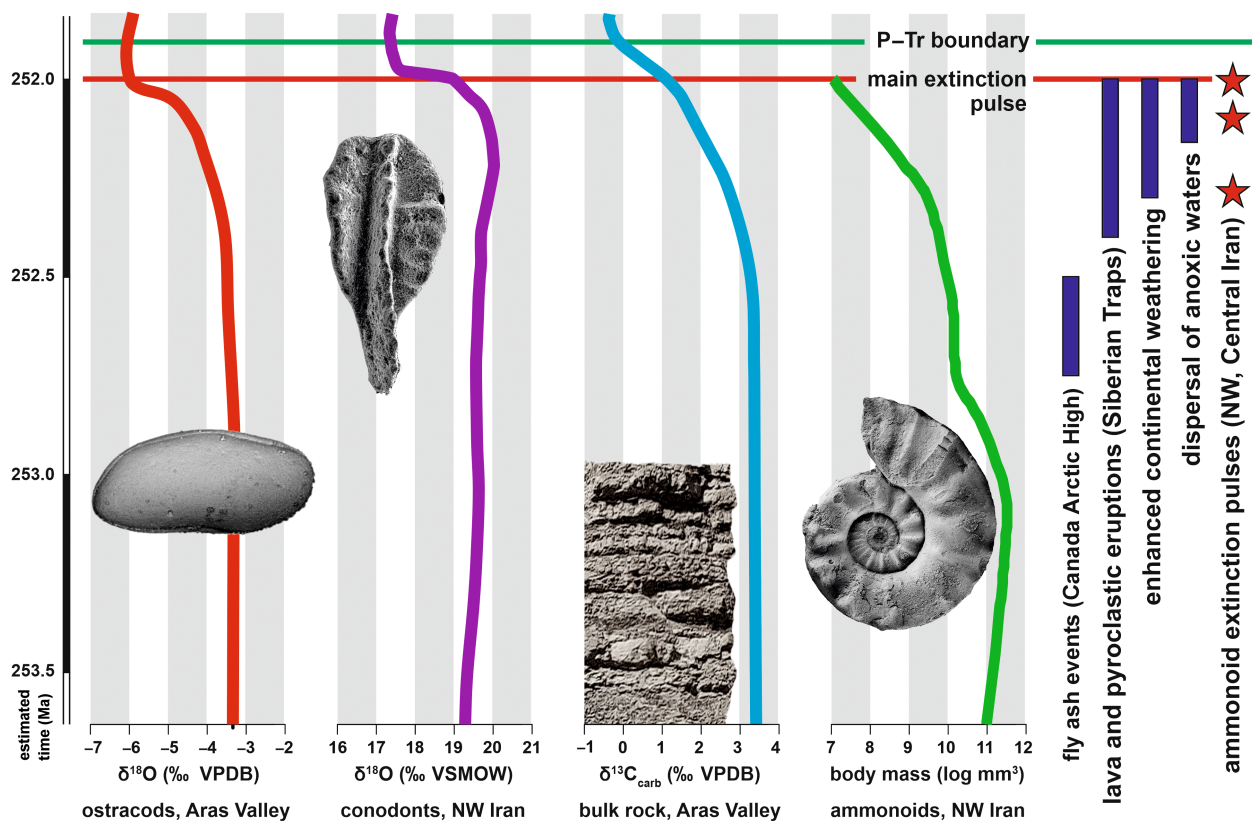
FIG. 4. Correlation of environmental and biotic changes. $\delta^{18}O$ (‰ VPDB) data from ostracod shell calcite from Aras Valley (this study) and $\delta^{18}O$ (‰ VSMOW) data from conodont apatite from Armenia and north-west Iran (Schobben *et al.* 2014; Joachimski *et al.* 2019); $\delta^{13}C_{carb}$ (‰ VPDB) data from bulk carbonate (Schobben *et al.* 2017); chamber volumes of ammonoids from north-west Iran (Kiessling *et al.* 2018); timing of environmental changes and volcanic activity (Brennecka *et al.* 2011; Grasby *et al.* 2011; Burgess & Bowring 2015; Schobben *et al.* 2015; Sun *et al.* 2018; Zhang *et al.* 2018); timing of ammonoid extinction pulses from Kiessling *et al.* (2018). LOESS smoothing and smoothing parameters as in Figures 2, 3 (smoothing parameter for chamber volume of ammonoids: 0.41). Ages estimated from reported sediment accumulation rates in north-west Iran (Schobben *et al.* 2015).

sharp temperature increase (Fig. 2), which corresponds to approximately 25 kyr before the main extinction pulse. This could represent a tipping point just prior to the main extinction. Similar data suggesting ecological shifts during this interval, which is characterized by a rather rapid temperature increase, are also recorded in the fossil record from South China. Palaeontological data indicate a decrease in body size of latest Changhsingian brachiopods (He *et al.* 2007; Zhang *et al.* 2016, 2017; He *et al.* 2017) as well as a decline in radiolarian diversity, just prior to the main extinction (Feng *et al.* 2007; Feng & Algeo 2014).

A temperature increase over a period of 300 kyr is likely to have influenced other environmental parameters of the oceanic realm. The expansion of anoxic waters, detected by independent proxies (Brennecka *et al.* 2011; Schobben *et al.* 2015, 2020; Zhang *et al.* 2018) began approximately 40–160 kyr before the extinction event (Zhang *et al.* 2018), with the maximum extent of anoxic waters occurring at the extinction horizon (Brennecka *et al.* 2011; Schobben *et al.* 2015). This timing suggests that only the last phase of temperature increase might have had a major influence on productivity, which indicates a tipping point being reached gradually rather than having been driven by very sudden global warming.

Our observation of gradual pre-mass extinction warming reconciles previously discrepant observations. Gradual pre-mass extinction warming explains biological responses before the main extinction horizon. It is likely that the main extinction pulse was triggered by threshold warming levels being gradually reached rather than a rapid, extreme warming disruption. As such, our study shows that gradual and relatively mild warming can be the canary in the coalmine of an approaching mass extinction. Permian life could not adapt to warming despite it having been spread out over hundreds of thousands of years.

As a final observation, we found no support for a transient cooling near the Permian–Triassic boundary as has been suggested based on the chronology of sea-level changes in South China (Baresel *et al.* 2017).

CONCLUSIONS

The end-Permian mass extinction has usually been linked to rapid global warming. In our study we challenge the previously proposed hypothesis that a geologically rapid (<40 kyr) temperature increase of more than 10°C occurred simultaneously to the main extinction pulse.

We studied the section spanning the latest Permian to earliest Triassic at the Aras Valley (north-west Iran) with respect to the oxygen isotope ratios in ostracod shells using secondary ion mass spectrometry (SIMS). Our study revealed the following main conclusions:

1. The ostracod shells of the Permian–Triassic boundary section of the Aras Valley (north-west Iran) are well preserved and are suitable for oxygen isotope measurements using a SIMS-based approach, which allows one to avoid altered, and overgrowth, diagenetic carbonates.

2. The geochemical (oxygen isotope) data indicate profound environmental disturbances prior to the main extinction pulse, evidenced by the negative excursion of the $\delta^{18}O_{ostr}$ values by 2.7‰ of the single ostracod species *Fabalicypris obunca*.

3. The measured oxygen isotope compositions of the ostracod shells support an increase in seawater temperatures beginning at least 300 kyr prior to the main extinction event (i.e. in the *Clarkina yini* Zone of the conodont stratigraphy). High temperatures persisted at least into at least into the *Isarcicella isarcica* Zone.

4. Gradual warming by approximately 12°C was probably responsible for initial environmental degradation culminating in the global, end-Permian biotic crisis.

Author contributions. JG, DK, MS and WK developed the conception and design of the work and carried out the interpretation of the data. JG, AG, MS, and DK collected the investigated material in the field. US performed the IRMS analysis of carbonate carbon isotopes. JG carried out the ostracod sample preparation. MW performed the ostracod SIMS analyses and undertook the quality assurance oversight. CU and MS provided the brachiopod isotope analysis of the Iranian material. JG, MW, DK and WK wrote the manuscript, and all the authors discussed the results, contributed to the interpretation of the data and to the final manuscript.

DATA ARCHIVING STATEMENT

Data for this study are available in the Dryad Digital Repository: https://doi.org/10.5061/dryad.f7m0cfxzw

Editor. Michael Hautmann

SUPPORTING INFORMATION

Additional Supporting Information can be found online (https://doi.org/10.1111/pala.12621):

Appendix S1. Supplementary methods and Figures S1–S3.

Fig. S1. SIMS sample mounts with polished surface. Gold-coated SIMS sample mounts after SIMS analyses with ostracod carapaces and crystal grains of reference material embedded in epoxy resin. Black scale bars indicate 5 mm.

Fig. S2. Influence of acetolysis on $\delta^{18}O_{ostr}$ and $\delta^{18}O_{spar}$ values. Measurements of orange boxplots represent the samples treated with water; blue boxplots represent the same sample material treated with acetolysis. Differences in $\delta^{18}O$ between the treatment methods are not significant for the shell calcite (p-value > 0.05, mean values for ostracod shell calcite: $-5.80‰$ and $-5.94‰$, median values: $-5.67‰$ and $-5.86‰$) and the sparite infilling of the carapaces (p-value > 0.05, mean values for sparite infilling: $-8.15‰$ and $-8.50‰$, median values: $-8.25‰$ and $-8.36‰$).

Fig. S3. Comparison of different stable isotope signals from the Aras Valley section. (A) $\delta^{13}C_{carb}$ data (Bennett *et al.* 2011) from bulk carbonate showing the beginning of the negative excursions in the *Clarkina yini* Zone. (B) $\delta^{18}O_{ostr}$ SIMS data from ostracod shell calcite showing a trend largely parallel to the $\delta^{13}C_{carb}$ data. Each data point of $\delta^{18}O_{ostr}$ is the arithmetic mean of all shell values measured from one specimen. (C) $\delta^{18}O_{bulk}$ values from bulk carbonate (Schobben *et al.* 2017). (D) $\delta^{18}O_{spar}$ SIMS values from sparite filling of the ostracod carapaces show a completely different isotopic compositions compared to the $\delta^{18}O_{ostr}$ data. Radiometric ages of the extinction horizon and first appearance of *Hindeodus parvus* at the Induan Stage GSSP (Meishan) (Burgess *et al.* 2014); approximated age of initial decrease of $\delta^{13}C_{carb}$ and $\delta^{18}O_{ostr}$ values based on the age model of Schobben *et al.* (2014) indicated in parenthesis. LOESS regression curves for temperature reconstructions of each dataset were calculated with a span of 0.5.

REFERENCES

BARESEL, B., BUCHER, H., BAGHERPOUR, B., BROSSE, M., GUODUN, K. and SCHALTEGGER, U. 2017. Timing of global regression and microbial bloom linked with the Permian-Triassic boundary mass extinction: implications for driving mechanisms. *Scientific Reports*, **7**, 43630.

BELOUSOVA, Z. D. 1965. Podklass Ostracoda. 254–265. *In:* RUZHENCEV, V.E. & SARYTCHEVA, T.G. (Eds.) *Rasvitie i smena morskikh organizmov na rubezhe Paleozoya i Mezozoya*. Trudy Paleontologicheskogo Instituta Akademiya Nauk SSSR, **108**. [in Russian]

BENTON, M. J. 2018. Hyperthermal-driven mass extinctions: killing models during the Permian–Triassic mass extinction. *Philosophical Transactions of the Royal Society A: Mathematical, Physical & Engineering Sciences*, **376**, 20170076.

BOND, D. P. and GRASBY, S. E. 2017. On the causes of mass extinctions. *Palaeogeography, Palaeoclimatology, Palaeoecology*, **478**, 3–29.

BORNEMANN, A., PIRKENSEER, C. M., DE DECKKER, P. and SPEIJER, R. P. 2012. Oxygen and carbon isotope fractionation of marine ostracod calcite from the eastern Mediterranean Sea. *Chemical Geology*, **310**, 114–125.

BRAND, U. and VEIZER, J. 1981. Chemical diagenesis of a multicomponent carbonate system; 2, Stable isotopes. *Journal of Sedimentary Research*, **51**, 987–997.

BRENNECKA, G. A., HERRMANN, A. D., ALGEO, T. J. and ANBAR, A. D. 2011. Rapid expansion of oceanic anoxia immediately before the end-Permian mass extinction. *Proceedings of the National Academy of Sciences*, **108**, 17631–17634.

BURGESS, S. D. and BOWRING, S. A. 2015. High-precision geochronology confirms voluminous magmatism before, during, and after Earth's most severe extinction. *Science Advances*, **1**, e1500470.

BURGESS, S. D., BOWRING, S. and SHEN, S. 2014. High-precision timeline for Earth's most severe extinction. *Proceedings of the National Academy of Sciences*, **111**, 3316–3321.

BURGESS, S., MUIRHEAD, J. and BOWRING, S. 2017. Initial pulse of Siberian Traps sills as the trigger of the end-Permian mass extinction. *Nature Communications*, **8**, 164.

CHEN, B., JOACHIMSKI, M. M., SHEN, S., LAMBERT, L. L., LAI, X., WANG, X., CHEN, J. and YUAN, D. 2013. Permian ice volume and palaeoclimate history: oxygen isotope proxies revisited. *Gondwana Research*, **24**, 77–89.

CHEN, J., SHEN, S., LI, X., XU, Y., JOACHIMSKI, M. M., BOWRING, S. A., ERWIN, D. H., YUAN, D., CHEN, B. and ZHANG, H. 2016. High-resolution SIMS oxygen isotope analysis on conodont apatite from South China and implications for the end-Permian mass extinction. *Palaeogeography, Palaeoclimatology, Palaeoecology*, **448**, 26–38.

CLAPHAM, M. E. and RENNE, P. R. 2019. Flood basalts and mass extinctions. *Annual Review of Earth & Planetary Sciences*, **47**, 275–303.

CLARKSON, M., KASEMANN, S. A., WOOD, R., LENTON, T., DAINES, S., RICHOZ, S., OHNEMUELLER, F., MEIXNER, A., POULTON, S. W. and TIPPER, E. 2015. Ocean acidification and the Permo-Triassic mass extinction. *Science*, **348**, 229–232.

CRASQUIN, S., PERRI, M. C., NICORA, A. and DE WEVER, P. 2008. Ostracods across the Permian–Triassic boundary in Western Tethys: the Bulla parastratotype (Southern Alps, Italy). *Rivista Italiana di Paleontologia e Stratigrafia*, **114**, 233–262.

CRASQUIN-SOLEAU, S., MARCOUX, J., ANGIOLINI, L., RICHOZ, S., NICORA, A., BAUD, A. and BERTHO, Y. 2004. A new ostracode fauna from the Permian–Triassic boundary in Turkey (Taurus, Antalya Nappes). *Micropaleontology*, **50**, 281–295.

CRASQUIN-SOLEAU, S., VASLET, D. and LE NINDRE, Y.-M. 2005. Ostracods as markers of the Permian/Triassic boundary in the Khuff Formation of Saudi Arabia. *Palaeontology*, **48**, 853–868.

CUI, Y. and KUMP, L. R. 2015. Global warming and the end-Permian extinction event: proxy and modeling perspectives. *Earth-Science Reviews*, **149**, 5–22.

DECROUY, L., VENNEMANN, T. W. and ARIZTEGUI, D. 2011. Controls on ostracod valve geochemistry: Part 2. Carbon and oxygen isotope compositions. *Geochimica et Cosmochimica Acta*, **75**, 7380–7399.

DEVRIENDT, L. S., McGREGOR, H. V. and CHIVAS, A. R. 2017. Ostracod calcite records the $^{18}O/^{16}O$ ratio of the bicarbonate and carbonate ions in water. *Geochimica et Cosmochimica Acta*, **214**, 30–50.

FENG, Q. and ALGEO, T. J. 2014. Evolution of oceanic redox conditions during the Permo-Triassic transition: evidence from deepwater radiolarian facies. *Earth-Science Reviews*, **137**, 34–51.

FENG, Q., HE, W., GU, S., MENG, Y., JIN, Y. and ZHANG, F. 2007. Radiolarian evolution during the latest Permian in South China. *Global & Planetary Change*, **55**, 177–192.

GHADERI, A., LEDA, L., SCHOBBEN, M., KORN, D. and ASHOURI, A. R. 2014. High-resolution stratigraphy of the Changhsingian (Late Permian) successions of NW Iran and the Transcaucasus based on lithological features, conodonts, and ammonoids. *Fossil Record*, **17**, 41–57.

GLIWA, J, GHADERI, A., LEDA, L., SCHOBBEN, M., TOMÁS, S., FOSTER, W. J., FOREL, M.-B., GHANIZADEH TABRIZI, N., GRASBY, S. E., STRUCK, U., ASHOURI, A. R. and KORN, D. 2020. Aras Valley (northwest Iran): high-resolution stratigraphy of a continuous central Tethyan Permian–Triassic boundary section. *Fossil Record*, **23**, 33–69.

GLIWA, J, FOREL, M.-B., CRASQUIN, S., GHADERI, A. and KORN, D. 2021. Ostracods from the end-Permian mass extinction in the Aras Valley section (Northwest Iran). *Papers in Palaeontology*, **7**, 1003–1047.

GLIWA, J, WIEDENBECK, M., SCHOBBEN, M., ULLMANN, C. V., KIESSLING, W., GHADERI, A., STRUCH, U. and KORN, D. 2022. Data from: Gradual warming prior to the end-Permian mass extinction. *Dryad Digital Repository*. https://doi.org/10.5061/dryad.f7m0cfxzw

GRASBY, S. E., SANEI, H. and BEAUCHAMP, B. 2011. Catastrophic dispersion of coal fly ash into oceans during the latest Permian extinction. *Nature Geoscience*, **4**, 104–107.

HE, W., SHI, G. R., FENG, Q., CAMPI, M. J., GU, S., BU, J., PENG, Y. and MENG, Y. 2007. Brachiopod miniaturization and its possible causes during the Permian–Triassic crisis in deep water environments, South China. *Palaeogeography, Palaeoclimatology, Palaeoecology*, **252**, 145–163.

HE, W., SHI, G. R., XIAO, Y., ZHANG, K., YANG, T., WU, H., ZHANG, Y., CHEN, B., YUE, M. and SHEN, J. 2017. Body-size changes of latest Permian brachiopods in varied palaeogeographic settings in South China and implications for controls on animal miniaturization in a highly stressed marine ecosystem. *Palaeogeography, Palaeoclimatology, Palaeoecology*, **486**, 33–45.

HOLLAND, S. M. and PATZKOWSKY, M. E. 2015. The stratigraphy of mass extinction. *Palaeontology*, **58**, 903–924.

HOLMES, J. A. and CHIVAS, A. R. 2002. Ostracod shell chemistry—overview. *In* J. A. HOLMES and A. R. CHIVAS (eds) *The Ostracoda: Applications in Quaternary Research*. American Geophysical Union, Geophysical Monograph Series, **131**. 185–204.

HUNT, G., WICAKSONO, S. A., BROWN, J. E. and MACLEOD, K. G. 2010. Climate-driven body-size trends in the ostracod fauna of the deep Indian Ocean. *Palaeontology*, **53**, 1255–1268.

IAEA 1993. Reference and intercomparison materials for stable isotopes of light elements. International Atomic Energy Agency. IAEA-TECDOC-825, 165 pp.

IAEA 2016. Reference sheet: Certified reference material IAEA-603 (calcite). International Atomic Energy Agency. RS_IAEA-603 [Rev.0], 7 pp.

JOACHIMSKI, M. M., LAI, X., SHEN, S., JIANG, H., LUO, G., CHEN, B., CHEN, J. and SUN, Y. 2012. Climate warming in the latest Permian and the Permian–Triassic mass extinction. *Geology*, **40**, 195–198.

JOACHIMSKI, M., ALEKSEEV, A., GRIGORYAN, A. and GATOVSKY, Y. A. 2019. Siberian Trap volcanism, global warming and the Permian-Triassic mass extinction: new insights from Armenian Permian-Triassic sections. *GSA Bulletin*, **132**, 427–443.

JURIKOVA, H., GUTJAHR, M., WALLMANN, K., FLÖGEL, S., LIEBETRAU, V., POSENATO, R., ANGIOLINI, L., GARBELLI, C., BRAND, U. and WIEDENBECK, M. 2020. Permian–Triassic mass extinction pulses driven by major marine carbon cycle perturbations. *Nature Geoscience*, **13**, 745–750.

KIDDER, D. L. and WORSLEY, T. R. 2004. Causes and consequences of extreme Permo-Triassic warming to globally equable climate and relation to the Permo-Triassic extinction and recovery. *Palaeogeography, Palaeoclimatology, Palaeoecology*, **203**, 207–237.

KIEHL, J. T. and SHIELDS, C. A. 2005. Climate simulation of the latest Permian: implications for mass extinction. *Geology*, **33**, 757–760.

KIESSLING, W., SCHOBBEN, M., GHADERI, A., HAIRAPETIAN, V., LEDA, L. and KORN, D. 2018. Pre–mass extinction decline of latest Permian ammonoids. *Geology*, **46**, 283–286.

KIM, S.-T. and O'NEIL, J. R. 1997. Equilibrium and nonequilibrium oxygen isotope effects in synthetic carbonates. *Geochimica et Cosmochimica Acta*, **61**, 3461–3475.

KÖNIGSHOF, P. 1992. Der Farbänderungsindex von Conodonten (CAI) in paläozoischen Gesteinen (Mitteldevon bis Unterkarbon) des Rheinischen Schiefergebirges—Eine Ergänzung zur Vitrinitreflexion. *Courier Forschungsinstitut Senckenberg*, **146**, 1–118.

KORN, D., GHADERI, A., LEDA, L., SCHOBBEN, M. and ASHOURI, A. R. 2016. The ammonoids from the Late Permian *Paratirolites* Limestone of Julfa (East Azerbaijan, Iran). *Journal of Systematic Palaeontology*, **14**, 841–890.

KORTE, C. and KOZUR, H. W. 2010. Carbon-isotope stratigraphy across the Permian–Triassic boundary: a review. *Journal of Asian Earth Sciences*, **39**, 215–235.

KORTE, C., JASPER, T., KOZUR, H. W. and VEIZER, J. 2005. $\delta^{18}O$ and $\delta^{13}C$ of Permian brachiopods: a record of seawater evolution and continental glaciation. *Palaeogeography, Palaeoclimatology, Palaeoecology*, **224**, 333–351.

LEDA, L., KORN, D., GHADERI, A., HAIRAPETIAN, V., STRUCK, U. and REIMOLD, W. U. 2014.

Lithostratigraphy and carbonate microfacies across the Permian–Triassic boundary near Julfa (NW Iran) and in the Baghuk Mountains (Central Iran). *Facies*, **60**, 295–325.

LHOMME, N., CLARKE, G. K. and RITZ, C. 2005. Global budget of water isotopes inferred from polar ice sheets. *Geophysical Research Letters*, **32**, 1–4.

PENN, J. L., DEUTSCH, C., PAYNE, J. L. and SPERLING, E. A. 2018. Temperature-dependent hypoxia explains biogeography and severity of end-Permian marine mass extinction. *Science*, **362**, eaat1327.

PÖRTNER, H. 2001. Climate change and temperature-dependent biogeography: oxygen limitation of thermal tolerance in animals. *Naturwissenschaften*, **88**, 137–146.

REICHOW, M. K., SAUNDERS, A. D., WHITE, R. V., PRINGLE, M. S., AL'MUKHAMEDOV, A. I., MEDVEDEV, A. I. and KIRDA, N. P. 2002. ^{40}Ar/^{39}Ar dates from the West Siberian Basin: Siberian flood basalt province doubled. *Science*, **296**, 1846–1849.

RICHOZ, S., KRYSTYN, L., BAUD, A., BRANDNER, R., HORACEK, M. and MOHTAT-AGHAI, P. 2010. Permian–Triassic boundary interval in the Middle East (Iran and N. Oman): progressive environmental change from detailed carbonate carbon isotope marine curve and sedimentary evolution. *Journal of Asian Earth Sciences*, **39**, 236–253.

SCHOBBEN, M., JOACHIMSKI, M. M., KORN, D., LEDA, L. and KORTE, C. 2014. Palaeotethys seawater temperature rise and an intensified hydrological cycle following the end-Permian mass extinction. *Gondwana Research*, **26**, 675–683.

SCHOBBEN, M., STEBBINS, A., GHADERI, A., STRAUSS, H., KORN, D. and KORTE, C. 2015. Flourishing ocean drives the end-Permian marine mass extinction. *Proceedings of the National Academy of Sciences*, **112**, 10298–10303.

SCHOBBEN, M., VAN DE VELDE, S., GLIWA, J., LEDA, L., KORN, D., STRUCK, U., ULLMAN, C. V., HAIRAPETIAN, V., GHADERI, A. and KORTE, C. 2017. Latest Permian carbonate carbon isotope variability traces heterogeneous organic carbon accumulation and authigenic carbonate formation. *Climate of the Past*, **13**, 1635–1659.

SCHOBBEN, M., VAN DE SCHOOTBRUGGE, B. and WIGNALL, P. B. 2019. Interpreting the carbon isotope record of mass extinctions. *Elements*, **15**, 331–337.

SCHOBBEN, M., FOSTER, W. J., SLEVELAND, A. R., ZUCHUAT, V., SVENSEN, H. H., PLANKE, S., BOND, D. P., MARCELIS, F., NEWTON, R. J. and WIGNALL, P. B. 2020. A nutrient control on marine anoxia during the end-Permian mass extinction. *Nature Geoscience*, **13**, 640–646.

STAMPFLI, G. M. and BOREL, G. D. 2002. A plate tectonic model for the Paleozoic and Mesozoic constrained by dynamic plate boundaries and restored synthetic oceanic isochrons. *Earth & Planetary Science Letters*, **196**, 17–33.

SUN, H., XIAO, Y., GAO, Y., ZHANG, G., CASEY, J. F. and SHEN, Y. 2018. Rapid enhancement of chemical weathering recorded by extremely light seawater lithium isotopes at the Permian–Triassic boundary. *Proceedings of the National Academy of Sciences*, **115**, 3782–3787.

SVENSEN, H., PLANKE, S., POLOZOV, A. G., SCHMIDBAUER, N., CORFU, F., PODLADCHIKOV, Y. and JAMTVEIT, B. 2009. Siberian gas venting and the end-Permian environmental crisis. *Earth & Planetary Science Letters*, **277**, 490–500.

VON GRAFENSTEIN, U., ERLERNKEUSER, H. and TRIMBORN, P. 1999. Oxygen and carbon isotopes in modern fresh-water ostracod valves: assessing vital offsets and autecological effects of interest for palaeoclimate studies. *Palaeogeography, Palaeoclimatology, Palaeoecology*, **148**, 133–152.

WANG, W., GARBELLI, C., ZHANG, F., ZHENG, Q., ZHANG, Y., YUAN, D., SHI, Y., CHEN, B. and SHEN, S. 2020. A high-resolution Middle to Late Permian paleotemperature curve reconstructed using oxygen isotopes of well-preserved brachiopod shells. *Earth & Planetary Science Letters*, **540**, 116245.

WATANABE, T., WINTER, A. and OBA, T. 2001. Seasonal changes in sea surface temperature and salinity during the Little Ice Age in the Caribbean Sea deduced from Mg/Ca and ^{18}O/^{16}O ratios in corals. *Marine Geology*, **173**, 21–35.

WESTERHOLD, T., MARWAN, N., DRURY, A. J., LIEBRAND, D., AGNINI, C., ANAGNOSTOU, E., BARNET, J. S., BOHATY, S. M., VLEESCHOUWER, D., FLORINDO, F., FREDERICHS, T., HODELL, D. A., HOLBOURN, A., KROON, D., LAURETANO, V., LITTLER, K., LOURENS, L. J., LYLE, M., PÄLIKE, H., RÖHL, U., TIAN, J., WILKENS, R. H., WILSON, P. A. and ZACHOS, J. C. 2020. An astronomically dated record of Earth's climate and its predictability over the last 66 Million Years. *Science*, **369**, 1383–1387.

WIGNALL, P. B. and TWITCHETT, R. J. 1996. Oceanic anoxia and the end Permian mass extinction. *Science*, **272**, 1155–1158.

XIA, J., ENGSTROM, D. and ITO, E. 1997. Geochemistry of ostracode calcite: Part 2. The effects of water chemistry and seasonal temperature variation on *Candona rawsoni*. *Geochimica et Cosmochimica Acta*, **61**, 383–391.

YUAN, D.-X., SHEN, S.-Z., HENDERSON, C. M., CHEN, J., ZHANG, H. and FENG, H.-Z. 2014. Revised conodont-based integrated high-resolution timescale for the Changhsingian Stage and end-Permian extinction interval at the Meishan sections, South China. *Lithos*, **204**, 220–245.

ZHANG, Y., SHI, G., HE, W.-H., WU, H.-T., LEI, Y., ZHANG, K.-X., DU, C.-C., YANG, T.-L., YUE, M.-L. and XIAO, Y.-F. 2016. Significant pre-mass extinction animal body-size changes: evidences from the Permian–Triassic boundary brachiopod faunas of South China. *Palaeogeography, Palaeoclimatology, Palaeoecology*, **448**, 85–95.

ZHANG, Y., SHI, G., WU, H.-T., YANG, T., HE, W., YUAN, A. and LEI, Y. 2017. Community replacement, ecological shift and early warning signals prior to the end-Permian mass extinction: a case study from a nearshore clastic-shelf section in South China. *Palaeogeography, Palaeoclimatology, Palaeoecology*, **487**, 118–135.

ZHANG, F., ROMANIELLO, S. J., ALGEO, T. J., LAU, K. V., CLAPHAM, M. E., RICHOZ, S., HERRMANN, A. D., SMITH, H., HORACEK, M. and ANBAR, A. D. 2018. Multiple episodes of extensive marine anoxia linked to global warming and continental weathering following the latest Permian mass extinction. *Science Advances*, **4**, e1602921.